AIMS Mathematics

AIMS Mathematics, 10(8): 17459–17482.
DOI: 10.3934/math.2025780
Received: 11 June 2025
Revised: 02 July 2025
Accepted: 04 July 2025
Published: 01 August 2025

http://www.aimspress.com/journal/Math

***Research article***

# Numerical analysis of heat transfer in a mixed-convection flow of drilling nanofluid embedded in a Darcy-Brinkman permeable medium with variables viscosity and thermal conductivity

**Fisal Asiri***

Department of Mathematics, Taibah University, Medina, 42353, Saudi Arabia

* **Correspondence:** Email: fahasiri@taibahu.edu.sa.

**Abstract:** This study investigates anomalous heat transfer in a radiative mixed convection flow of water-based drilling nanofluid (NF) immersed in a Darcy–Brinkman permeable medium. Since the underground fluids are exposed to anomalous temperatures, the extraction of gases and petroleum from rocks and soil requires the drilling fluids to have temperature-dependent viscosity and thermal conductivity. The variable thermal conductivity and viscosity of the drilling fluid provide resistance to high temperatures and pressure. Therefore, the objective of this study was to investigate anomalous heat transfer subject to frictional heating, melting heat, thermal radiation, and magnetic fields. Using the Brinkman–Maxwell–Garnett model, the effective thermophysical properties of drilling NF are considered. The computational performance of drilling NF is investigated using the Adams–Bashforth predictor and corrector approach. The findings suggest that the volume percentage and free convection parameter increases the Nusselt number considerably. The thickness of the boundary layer is increased by a higher permeability parameter, whereas the Darcy number exhibits the opposite tendency. Fluid velocity and skin friction are reduced by the magnetic number, whereas the temperature profile is raised by increases in the radiation parameter and the volume percentage of nanoparticles. The rate of heat transmission becomes significant in the scenario of variable characteristics.

**Keywords:** drilling nanofluid; clay and graphene nanomaterials; variable viscosity; thermal conductivity; free convection; nonlinear thermal radiation; melting heat

## 1. Introduction

In fluid dynamics, the boundary layer flow (BLF) over an expanding sheet is an important phenomenon that is frequently examined in the context of mass and heat transfer. A distinct flow pattern is produced when fluid flows over a stretched surface, resulting in an intersection of streamlines at a stagnation point (SP). Stretching sheets are used for industrial purposes, such as polymer processing, where it is essential to comprehend the fluid's behavior when stretching materials are present. The boundary layer (BL) formation, near the stagnation region under a varying stretching sheet is significant in modern industry. The SP has been a significant field of research for almost a century, drawing the interest of scientist/engineers because of its wide range of applications. The SP can be found in many different application areas, including the use of fans to cool electronics, emergency shutdown cooling in nuclear reactors, aerodynamic submarine and aircraft design, rocket tips' behavior in flight, wind currents' effects on fundamental solar receivers, and a variety of drilling processes that are essential to many different engineering applications. The investigation of fluid flow near the SP originated with the groundbreaking study of Hiemenz [1] in 1911. His findings play a leading role while addressing the two-dimensional (2D) SP flow (SPF) across a movable surface. Afterward, Homann [2] investigated the axisymmetric fluid flow in the vicinity of the SP. The Hiemenz-type flows characterize the most recent set of nonaxisymmetric SPFs, which is another prime outcome recognized by Howarth [3]. The exploration of three-dimensional (3D) SPFs was discussed by Davey and Schofield [4]. The SPF of nanofluid (NF) flowing across a stretching/shrinking plate was assessed by Bachok et al. [5]. Dash et al. [6] expanded the investigation of [5] by including SPFs past a stretching sheet.

Heat transfer (HT) frameworks have a significant impact on the performance and quality of the final product in an assortment of manufacturing sectors [7]. Fluids like alcohol, ethylene glycol, water, and oils were used before the development of NF, acting as an efficient heat transporters, allowing thermal energy to be transferred between various system components. Conduction, convection, and radiation are the three HT mechanisms that manufacturers can optimize to increase thermal management, energy efficiency, and the consistency of processing temperature, which ultimately improve performance and save operating costs. Choi and Eastman [8] proposed the concept of NF, a new class of heat-transferring fluids. Carbon nanotubes, silica, oxides, metallic compounds, and other minuscule particles combine to form NF. Scientists and industrialists are currently concentrating on the research and development of NF in order to address the issues related to HT in the industrial sectors. In a permeable medium with unpredictable radiation and chemical reaction effects, Liu et al. [9] examined the magnetic influence on the NF flowing across an extensible cylinder. In a permeable medium, Pattnaik et al. [10] examined the magnetohydrodynamic (MHD) axisymmetric flow of NF from a stretched cylinder. Sedki [11] investigated radiation-induced MHD mixed convective NF flow. The computational investigation of the radiative flow of non-Newtonian NF in the presence of gyrotactic microorganisms and activation energy was explored by Anjum et al. [12]. In an unsteady MHD Cattaneo–Christov flow in Oldroyd-B NF flow with slip impact was discussed by Bai et al. [13]. Bioconvective magnetized Williamson NF flow using radiation and activation energy was studied by Asjad et al. [14]. The effect of radiation on the convective flow of micropolar NF was examined by Mabood et al. [15]. The effects of activation energy and melting on MHD Reiner–Rivlin NF flow were discussed by Khan et al. [16]. Rehman et al. [17] investigated the enhancement of HT using Hybrid NanoFluid (HNF) comprising microorganisms over a linear sheet taking radiative HT. They introduced a novel parameter $N_{bt}$ (the Brownian to thermophoresis ratio) which frequently enhances the Nusselt number. Tian et al. [18] introduced the HT enhancement and entropy generation minimization mechanism using tri-HNF over a stretchable cylinder. They found that the fluid flow and HT rate were improved by elevating the fluid parameter and curvature of the cylinder. The HT rate was enriched in a thin film flow of micropolar NF taking Maxwell–Bruggeman and Krieger–Dougherty NF models, as revealed by Shen et al.'s study [19]. Their finding reveals that the HT rate increased significantly when the aggregation of nanomaterials was taken into consideration.

Clay nanoparticles (NPs) are increasingly used to improve the rheological features of drilling fluids in high-temperature and high-pressure settings [20]. Their unique features increase the drilling fluid's stability and viscosity, avoiding solidification and preserving ideal flow characteristics. These NPs ensure improved performance in difficult drilling situations by efficiently suspending cutting and minimizing fluid loss, which eventually leads to safer and more successful operations. High pressures and temperatures are experienced in deep drilling procedures, which produce an adverse effect on the efficacy of drilling fluids. A large amount of research has been done on the crucial impact of drilling fluids on drilling efficiency, but the temperature-dependent viscosity and thermal conductivity of drilling fluid has not been addressed before. Khan et al. [21] used clay NPs to investigate the convective heat transport of drilling fluid. The optimum thermal and physical properties of clay NFs were examined using the mathematical models developed by Maxwell-Garnett and Brinkman. In Cheraghian's investigation [22], clay NPs were introduced into drilling fluid, which increased the drilling fluid viscosity. A comparison of numerous different kinds of base fluids encompassing clay NPs was carried out by Nisar et al. [23]. They examined the number of parameters that resulted in the minimization of irreversibility. Elattar et al. [24] examined a Williamson drilling fluid using clay NPs over a flat surface occupied in a Darcy–Brinkman porous medium. Their results showed that when the volumetric concentration rises, the Nusselt number increases considerably. In a recent study, Isede and Adeniyan [25] explored the flow and HT features of drilling NF containing clay NPs subject to radiative HT. A few recent developments on drilling fluid containing clay NPs are explored in recent studies [26, 27]. Besides all these developments on the said problem, the temperature-dependent thermophysical features of drilling fluid, which is another important aspect, has not been taken into consideration, even though drilling fluids are exposed to high temperature and pressure below the Earth's surface.

The Darcy–Brinkman model (DBM) is frequently employed to explain fluid flow in materials that include both microscopic and macroscopic permeable structures, such as filters, biological tissues, and soils [28]. In order to account for the effects of the fluid's viscosity and the relationship between the fluid and the solid matrix, the Brinkman equation is combined with Darcy's law for slow, viscous flow through porous materials. This model offers insights into processes like HT in porous materials, contaminant transport, and groundwater movement, and it is especially helpful in situations involving flows with a low Reynolds number $(Re)$. Transportation and conserving energy are the usual applications of porous media. According to Darcy's law, the force of gravity and the pressure gradient have a linear relationship with the flow. For viscous liquids in permeable media at a low $Re$, when the medium is tightly packed (low porosity), this rule is commonly accepted as the momentum equation. The standard viscous resistance term, frequently referred to as the Brinkman term, is considered in conjunction with Darcy' resistance term [29]. Rosali et al. [30] investigated the buoyancy SPF across an upright plate submerged in a permeable medium with a constant heat flux. They found different solutions for buoyancy assisting and opposing the flow. The effect of suction and blowing on the erratic flow of a Maxwell fluid across a stretchable sheet imbedded in a permeable medium was examined by Mukhopadhyay [31]. He found that an increase in the Maxwell parameter suppresses the velocity field. The forced convection flow with mass and HT through a porous parallel channel plate was examined by Wang et al. [32]. Zaib et al. [33] examined the flow and HT of a Casson liquid in a DB permeable medium with slip effects across an upright plate. They discovered a distinct outcome for assisting flow and several outcomes for opposing flow. The forced convective flow in a rotating conduit in a DB permeable medium with was covered by Wang [34].

The goal of this study was to investigate the anomalous heat transfer of water-based drilling NF moving across an upright stretched surface dipped in a Darcy–Brinkman permeable medium. Drilling processes use drilling mud, which is composed of water-based clay nanomaterials. In order to increase the drilling efficiency, clay and graphene NPs are added to the water. Minimal torque, thermal stability, leakage prevention, suitable rheological characteristics for drilling hole extraction, and improved filtration are the core objectives of drilling engineers when performing drilling operations. Some modern drilling methods coat the drilling surface with a thin, stretchy layer of lubricant or coolant. This layer prolongs life and increases cutting efficiency by lowering heat generation and friction. Ensuring accuracy and avoiding destruction during high-speed or deep drilling operations depends on the stretching sheet's ability to distribute the fluid evenly, improve cooling, and remove chips. Very few studies [35,36] are available in recent literature; however, these studies are limited to reviews of other studies. This study provides new insight into the anomalous heat transfer performance of drilling NF flow containing clay and graphene NPs. Furthermore, temperature-dependent viscosity, thermal conductivity and a Darcy–Brinkman permeable medium are the novel aspects of this study. The melting heat at the surface, nonlinear thermal radiation, and frictional heating are included. A multistep computational approach (the Adam–Bashforth approach, which relies on the predictor and corrector technique) is implemented for the numerical results. A comparison of the frictional drag coefficient and Nusselt number with constant and variable viscosity and thermal conductivity is provided.

At the end of the mathematical analysis, we will be able to answer the following research questions:

- How is the anomalous heat transfer performance in water-based drilling NF enhanced with the addition of clay and graphene NPs?
- How does the heat transfer properties of drilling NF flowing over a vertical surface immersed in a Darcy–Brinkman permeable medium rely on temperature-dependent viscosity and thermal conductivity?
- How can nonlinear thermal radiation, frictional heating, and melting heat at the surface impact the drilling NF's thermal stability and effectiveness?
- How do radiation, magnetic factors, changed porosity, free convection, Darcy number, and melting heat affect the skin friction and heat transfer rate during drilling?

## 2. Materials and methods

### *2.1. Mathematical background of the model and analysis*

The BLF of drilling NF, which is mixture of clay and graphene NPs near the SP are displayed in Figure 1(a). We have assumed mixed radiative convection and an incompressible flow of water-based NF past a vertical stretchable surface. The surface is oriented in such a way that the sheet is located along the $x$ −axis, while the flow originates along the $y$ −axis due to surface stretching with a velocity $u_w(x) = ax$. A strong magnetic field $B = B_0$ acts normal to the flow field.

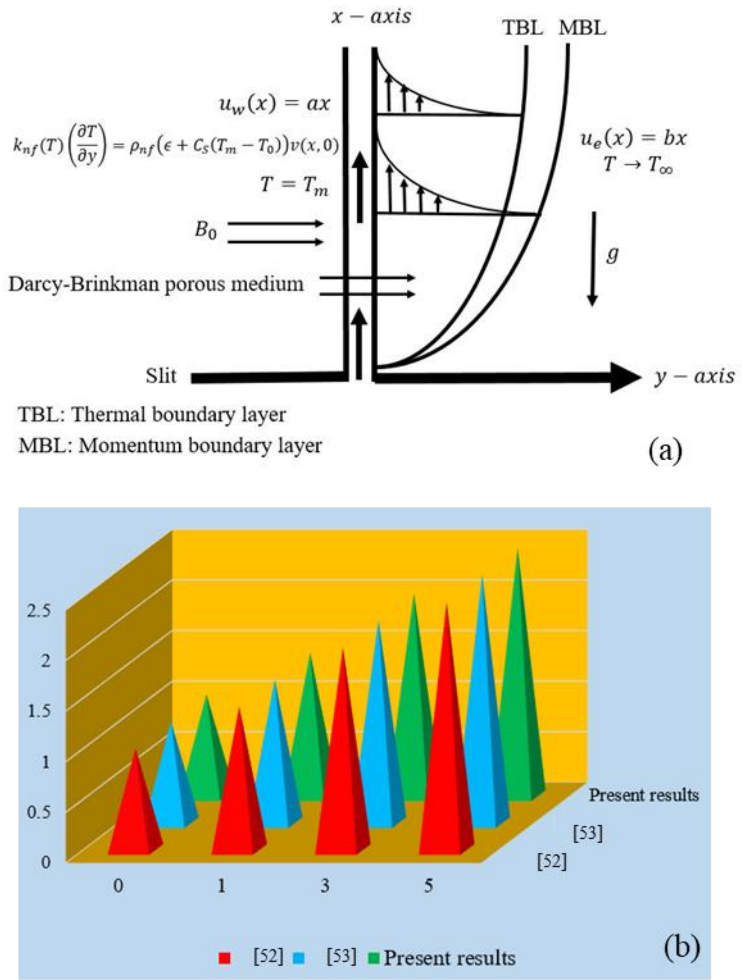


**Figure 1.** (a) Physical description of the model, (b) Model validation chart.

In order to simplify the flow models some essential assumptions are made:

- The flow is a BLF.
- A Darcy–Brinkman permeable medium is considered, which accounts for the porosity and permeability of the permeable medium.
- Nonlinear thermal radiation is assumed to account for practical scenarios in high-temperature drilling.
- Temperature-dependent viscosity and thermal conductivity are considered.
- There is a buoyancy assisting flow scenario due to $(T - T_\infty)$.
- Clay–graphene NPs with equal friction are dispersed in a drilling fluid (water).
- Boussinesq approximation is implemented.
- Viscous dissipation, Joule heating, and melting heat at the surface are assumed.
- The wall and free stream velocities are taken as $u_w(x) = ax$ and $u_e(x) = bx$, respectively, where $a, b > 0$, indicating the stretching rate.

- The surface and far field temperature are assumed to be $T_m$ and $T_\infty$,defining the melting surface temperature and ambient temperature.

The governing BL flow equation accounting for these assumptions is as follows [24,36,37]:

$$\frac{\partial u}{\partial x}+\frac{\partial v}{\partial y}=0, \tag{1}$$

$$\frac{\rho_{nf}}{\gamma_p^2}\left(u\frac{\partial u}{\partial x}+v\frac{\partial u}{\partial y}\right)=\left(\left(\frac{\partial \mu_{nf}(T)}{\partial y}\right)\frac{\partial u}{\partial y}+\mu_{nf}(T)\frac{\partial^2 u}{\partial y^2}\right)+u_e(x)\frac{du_e(x)}{dx}-\frac{\mu_{nf}(T)}{\rho_{nf}K_P}\left(u-u_e(x)\right)-\sigma_{nf}(T)B_0^2\left(u-u_e(x)\right)+g(\rho\beta)_{nf}(T-T_\infty), \tag{2}$$

$$\left(u\frac{\partial T}{\partial x}+v\frac{\partial T}{\partial y}\right)=\frac{1}{(\rho c_p)_{nf}}\left(\frac{\partial k_{nf}(T)}{\partial y}\frac{\partial T}{\partial y}+k_{nf}(T)\frac{\partial^2 T}{\partial y^2}\right)-\frac{1}{(\rho c_p)_{nf}}\frac{\partial q_r}{\partial y}+\frac{\sigma_{nf}(T)B_0^2}{(\rho c_p)_{nf}}\left(u-u_e(x)\right)^2+\frac{1}{(\rho c_p)_{nf}}\left(\left(\frac{\partial \mu_{nf}(T)}{\partial y}\right)\left(\frac{\partial u}{\partial y}\right)^2+\mu_{nf}(T)\left(\frac{\partial u}{\partial y}\right)^3\right), \tag{3}$$

subject to the following surface and far field constraints [38–40]:

$$\text{at } y\to 0:\ u=u_w(x)=ax,\ k_{nf}(T)\left(\frac{\partial T}{\partial y}\right)=\rho_{nf}\left(\epsilon+C_S(T_m-T_0)\right)v(x,0),\ T=T_m, \tag{4}$$

$$\text{at } y\to\infty:\ u\to u_e(x)=bx,\ T\to T_\infty. \tag{5}$$

In the governing equations above, $\in_d$ is the permeability of the medium, $\rho_{nf}$ is the density of the NF, $K_P$ is the porosity of the porous medium, $(\rho\beta)_{nf}$ is the coefficient of the thermal expansion, and $g=9.8m/s^2$ is gravitational acceleration. Furthermore, $T_m$ and $T_0$ are the melting and reference temperatures, respectively, and $C_S$ indicates the heat capacitance of a solid surface.

The effective use of nonlinear thermal radiation in drilling fluids improves the thermal conductivity with the distribution of NPs, increasing the effectiveness of heat dissipation in high-temperature boreholes. Its temperature-dependent radiative flux reduces the risk of overheating during deep drilling operations, while also decreasing fluid deterioration and machine wear.

Here, $q_r$ is the nonlinear thermal radiation [41,42]. Using Rosseland's approximation for $q_r$ [43], it is defined as

$$q_r=-\frac{4\sigma^*}{3k^*}\frac{\partial T^4}{\partial y}=-\frac{16\sigma^*}{3k^*}T^3\frac{\partial T}{\partial y}. \tag{6}$$

Assuming that there is a significant fluctuation in the temperature within in flow field, the expression $T$ may be expressed as

$$\frac{\partial q_r}{\partial y}=-\frac{16\sigma^*}{3k^*}\left(3T^2\left(\frac{\partial T}{\partial y}\right)^2+T^3\frac{\partial^2 T}{\partial y^2}\right), \tag{7}$$

where $\sigma^*$ and $k^*$ are the Stefan–Boltzmann constant and the mean absorption coefficient, respectively.

The expressions $\mu_{nf}(T)$, $k_{nf}(T)$ and $\sigma_{nf}(T)$ are the temperature-dependent viscosity and thermal and electrical conductivity of NF, respectively. Their formulations are given below [36,44]

$$\sigma_{nf}(T)=\sigma_f\left(1+\delta_1\left(\frac{(T-T_0)}{(T_m-T_0)}\right)\right), \tag{8}$$

$$\mu_{nf}(T)=\mu_f\left(1+\delta_2\left(\frac{(T-T_0)}{(T_m-T_0)}\right)\right), \tag{9}$$

$$k_{nf}(T)=k_f\left(1+\delta_3\left(\frac{(T-T_0)}{(T_m-T_0)}\right)\right). \tag{10}$$

The characteristics of NF are defined according to the Brinkman–Maxwell–Garnett model [19]:

$$\frac{\rho_{nf}}{\rho_f}=\left(1-\varphi+\varphi\frac{\rho_s}{\rho_f}\right), \frac{(\rho\beta)_{nf}}{(\rho\beta)_f}=1-\varphi+\varphi\frac{(\rho\beta)_s}{(\rho\beta)_f}, \frac{(\rho c_p)_{nf}}{(\rho c_p)_f}=1-\varphi+\varphi\frac{(\rho c_p)_s}{(\rho c_p)_f}, \tag{11}$$

where $\varphi$ is the volumetric percentage of solid particles, and the subscript $s$ and $f$ indicate the solid nanomaterials and the working fluid, respectively.

Incorporating the similarity variables [19,45,46], we have

$$\eta=y\sqrt{\frac{a}{\nu}}, \psi=\sqrt{a\nu}xF(\eta), \Theta(\eta)=\frac{T-T_\infty}{T_w-T_\infty}. \tag{12}$$

In light of the stream function $u=\frac{\partial\psi}{\partial y}, v=-\frac{\partial\psi}{\partial x}$, the components of velocity take the following form:

$$u=axF'(\eta), v=-\sqrt{a\nu}F(\eta). \tag{13}$$

Using Eqs (10) and (11) in the governing equations above, we get

$$\begin{aligned}&\frac{\mu_{nf}/\mu_f}{\rho_{nf}/\rho_f}\varepsilon_A(1-\alpha_1\Theta)F'''-\alpha_1\Theta'F''+FF''-F'^2+\frac{\mu_{nf}/\mu_f}{\rho_{nf}/\rho_f}Da^{-1}(A^2-F')+\varepsilon_A(A^2-F'^2)+\\&\frac{(\rho\beta)_{nf}/(\rho\beta)_f}{\rho_{nf}/\rho_f}Gr\Theta-M\frac{\sigma_{nf}/\sigma_f}{\rho_{nf}/\rho_f}(1+\omega_1\Theta)(A^2-F')+A^2=0,\end{aligned} \tag{14}$$

$$\begin{aligned}&\frac{1}{\frac{(\rho c_p)_{nf}}{(\rho c_p)_f}}\left(\frac{k_{nf}}{k_f}+\frac{4}{3}Nr\right)(1+\beta_1\Theta)\Theta''+\beta_1\Theta'^2+PrF\Theta'+PrF'\\&+\frac{1}{(\rho c_p)_{nf}/(\rho c_p)_f}\left(\frac{4}{3}Nr(\Theta_w-1)^3(3\Theta^2(\Theta')^2+\Theta^3\Theta'')\right.\\&\left.+3(\Theta_w-1)^2(2\Theta(\Theta')^2+\Theta^2\Theta'')+3(\Theta_w-1)((\Theta')^2+\Theta\Theta'')\right)\\&+\frac{\mu_{nf}/\mu_f}{(\rho c_p)_{nf}/(\rho c_p)_f}(1+\alpha_1\Theta)PrEc(F''^2+F''^3)\\&+\frac{\sigma_{nf}/\sigma_f}{(\rho c_p)_{nf}/(\rho c_p)_f}PrEcM(1+\omega_1\Theta)(A^2-F')^2=0\end{aligned} \tag{15}$$

with

$$F'(0) = 1, \frac{\mu_{nf}}{\mu_f} PrF(0) + \frac{(\rho c_p)_{nf}}{(\rho c_p)_f} M_e \Theta'(0) = 0, \Theta(0) = 1, \tag{16}$$

$$F'(\infty) = A, \Theta(\infty) = 0, \tag{17}$$

where $\varepsilon_A = \gamma_p \frac{\mu_{eff}}{\mu_f}$ denotes the porosity parameter of the permeable medium, $Da^{-1} = \gamma_p^2 \frac{\nu_f}{aK}$ is the Darcy number, $M = \frac{\sigma_f B_0^2}{\rho_f a}$ is the magnetic parameter, $A = \frac{b}{a}$ denotes the stretching ratio, $M_e = \frac{(c_p)_f (T_w - T_\infty)}{\epsilon + C_S (T_m - T_w)}$ is the melting heat parameter, $\Theta_w = \frac{T_w}{T_\infty}$ is the temperature ratio, $Nr = \frac{16\sigma^*}{3k_f k^*} T_\infty^3$ denotes the radiative parameter, $Pr = \frac{\mu_f (c_p)_f}{k_f}$ is the Prandtl number, $Ec = \frac{u_w^2}{\rho c_p (T_w - T_\infty)}$, is the Eckert number, $Gr = \frac{g(\rho\beta)(T_w - T_\infty)}{\nu_f{}^2}$ is the thermal Grashof number, $\Delta_1 = \frac{Gr}{Re^2{}_x}$ is the free convection parameter, and $Re_x = \frac{u_w x}{\nu_f}$ is the Reynolds number. Furthermore, $\alpha_1 = \frac{(T_w - T_\infty)}{(T_m - T_w)}$, $\beta_1 = \frac{(T_w - T_\infty)}{(T_m - T_w)}$, and $\omega_1 = \frac{(T_w - T_\infty)}{(T_m - T_w)}$ are the temperature-dependent viscosity, thermal conductivity and electrical conductivity parameters, respectively.

The physical quantitates (skin friction $C_{fx}$ and heat transfer $Nu_x$) related to this model are provided in the following equations:

$$C_{fx} = \frac{2\mu_{nf}(T)\left(\frac{\partial u}{\partial y}\right)\Big|_{y=0}}{\rho_f u_w^2}, \tag{18}$$

$$Nu_x = \frac{-x}{k_{nf}(T)(T_w - T_\infty)} \frac{16\sigma^*}{3k^*} T^3 \frac{\partial T}{\partial y}\Big|_{y=0}. \tag{19}$$

In dimensionless form

$$\frac{1}{2}\sqrt{Re_x} Cf = \frac{\mu_{hnf}}{\mu_f} (1 - \alpha_1 \Theta) f''(0), \tag{20}$$

$$\frac{Nu}{\sqrt{Re_x}} = -\left(\frac{k_{hnf}}{k_f}\big(1 + \beta_1 \Theta(0)\big) + \frac{4}{3} Nr\big(1 + (\Theta_w - 1)\Theta(0)\big)^3\right)\big(\Theta'(0)\big). \tag{21}$$

The thermophysical properties of the dispersed nanomaterials are given in Table 1 [47–49].

**Table 1.** Details of dispersed nanomaterials taking $Pr = 6.2$, at room temperature (28 °C).

| **Materials** | $c_p$: $[J.kg^{-1}.K^{-1}]$ | $\rho$: $[kg.m^{-3}]$ | $k$: $[W.m^{-1}.K^{-1}]$ | $\beta$: $[10^{-5}K^{-1}]$ | $\sigma$: $[S.m^{-1}.]$ |
|---|---|---|---|---|---|
| **Water** | 4179 | 997 | 0.613 | 21 | 0.005 |
| **Clay nanoparticles** | 531.8 | 6320 | 76.5 | 1.80 | $10^{-7}$ |
| **Graphene oxide ($Go$)** | 2100 | 2250 | 2500 | 0.284 | $10^{7}$ |

### 2.2. Solution methodology

The numerical method for solving our nondimensional system in (14) and (15) under the specified boundary conditions of (16) and (17) is addressed in this section. For this purpose, we employed the numerical approach of the linear multistep Adams–Bashforth (AB) predictor–corrector (PC) method [50]. By preserving and utilizing prior information regarding the phases instead of discarding it, multistep techniques aim to enhance performance, resulting in a large number of prior points and derivative values. It works in two stages. Initially, we use the AB approach to estimate the necessary value as a prediction phase. The Adams–Moulton technique is then used as a corrector step to rectify the first approximation. The AB method can be extended to higher orders by incorporating more past points, allowing the user to choose a compromise between precision and processing efficiency according to the needs of the scenario [51]. The PC systems, which use an implicit methodology to correct the initial prediction of an explicit method, are integrated with the AB procedures. The following variables are introduced in order to reduce the system to the first order:

$$\mathbb{U}_1 = F, \mathbb{U}_2 = F', \mathbb{U}_3 = F'', \mathbb{U}_4 = \Theta, \mathbb{U}_5 = \Theta', \tag{22}$$

$$\begin{gathered}\mathbb{U}_3' = \alpha_1 \mathbb{U}_5 \mathbb{U}_3 - \mathbb{U}_1 \mathbb{U}_3 + {\mathbb{U}_2}^2 - \frac{\frac{\mu_{nf}}{\mu_f}}{\frac{\rho_{nf}}{\rho_f}} Da^{-1} \left(A^2 - \mathbb{U}_2\right) - \varepsilon_A \left(A^2 - {\mathbb{U}_2}^2\right) - \frac{\frac{(\rho\beta)_{nf}}{(\rho\beta)_f}}{\frac{\rho_{nf}}{\rho_f}} Gr \mathbb{U}_4 + \\ M \frac{\frac{\sigma_{nf}}{\sigma_f}}{\frac{\rho_{nf}}{\rho_f}} (1 + \omega_1 \mathbb{U}_4) \left(A^2 - \mathbb{U}_2\right) - A^2,\end{gathered} \tag{23}$$

$$\mathbb{U}_5' = - \frac{\begin{pmatrix} \beta_1 {\mathbb{U}_5}^2 + Pr \mathbb{U}_1 \mathbb{U}_5 + Pr \mathbb{U}_2 + \frac{1}{\frac{(\rho c_p)_{nf}}{(\rho c_p)_f}} 4Nr(\Theta_w - 1)^3 {\mathbb{U}_4}^2 {\mathbb{U}_5}^2 + 3(\Theta_w - 1)^2 2\mathbb{U}_4 {\mathbb{U}_5}^2 + 4(\Theta_w - 1){\mathbb{U}_5}^2 + \\ \frac{\mu_{nf}/\mu_f}{(\rho c_p)_{nf}/(\rho c_p)_f} (1 + \alpha_1 \mathbb{U}_4) Pr Ec \left({\mathbb{U}_3}^2 + {\mathbb{U}_5}^3\right) + \frac{\sigma_{nf}/\sigma_f}{(\rho c_p)_{nf}/(\rho c_p)_f} Pr Ec M (1 + \omega_1 \mathbb{U}_4) \left(A^2 - \mathbb{U}_2\right)^2 \end{pmatrix}}{\frac{1}{\frac{(\rho c_p)_{nf}}{(\rho c_p)_f}} \left( \left( \frac{k_{nf}}{k_f} + \frac{4}{3} Nr \right) (1 + \beta_1 \mathbb{U}_4) + \frac{4}{3} Nr (\Theta_w - 1)^3 {\mathbb{U}_4}^3 + 4Nr(\Theta_w - 1)^2 {\mathbb{U}_4}^2 + 4(\Theta_w - 1)\mathbb{U}_4 \right)}, \tag{24}$$

with (24)

$$\mathbb{U}_2(0) = 1, \frac{\mu_{nf}}{\mu_f} Pr \mathbb{U}_1(0) + \frac{(\rho c_p)_{nf}}{(\rho c_p)_f} M_e \mathbb{U}_5(0) = 0, \mathbb{U}_4(0) = 1, \tag{25}$$

$$\mathbb{U}_2(\infty) = A, \mathbb{U}_4(\infty) = 0. \tag{26}$$

Considering that this is multistep numerical process known as PC, the predictor formula is

$$y_{m+1,P} = y_m + \frac{h}{24}(55 y_m' - 59 y_{m-1}' + 37 y_{m-2}' - 9 y_{m-3}'), \tag{27}$$

and the corrector formula is

$$y_{m+1,C} = y_m + \frac{h}{24}(9 y_{m+1}' - 59 y_m' + 37 y_{m-1}' - 9 y_{m-2}'). \tag{28}$$

The results are compared using a small number $\varepsilon$ after subtracting the boundary conditions from the predicted and corrected values that are derived from the AB formulas. We choose an alternative guess and repeat the same process if the numbers are greater than $\varepsilon$. If the values are less than $\varepsilon$, the desired results are correct. If the obtained values are not smaller than $\varepsilon$ once again, we employ the secant approach to improve our estimations. The process continues until the boundary condition is met. This approach produces numerical solutions with the highest precision and improved convergence. Fourth-order convergence is obtained.

A comparison of the validity of the current model for skin friction with the results of Nadeem et al. [52] and Khan et al. [53] is provided in Figure 1(b). The model validation for the Nusselt number is provided in Tables 2 and 3, compared with the results of Hayat et al. [54], Dogonchi et al. [55], and Rashidi et al. [56].

**Table 2.** Comparison of the Nusselt number $\Theta'(0)$ with the results of Hayat et al. [54] taking $\Theta_w = 0, Nr = 0, Ec = 0, \beta_1 = 0, \alpha_1 = 0, \varphi = 0,$ and $A = 0$.

| $Pr$ | $M_e$ | Hayat et al. [54] | Present results |
|---|---|---|---|
| **1.0** | 0.0 | 0.64944 | 0.64939 |
| | 0.3 | 0.54788 | 0.54767 |
| | 0.5 | 0.49871 | 0.49858 |
| | 0.8 | 0.44139 | 0.44124 |
| **0.8** | 0.5 | 0.43557 | 0.43546 |

**Table 3.** Comparison of the Nusselt number $\Theta'(0)$ with the results of Dogonchi et al. [55] taking $\Theta_w = 0, Ec = 0, \beta_1 = 0, \alpha_1 = 0, \varphi = 0,\ and A = 0$.

| | Rashidi et al. [56] | | Dogonchi et al. [55] | | Present results | |
|---|---|---|---|---|---|---|
| $Nr$ | $f''(0)$ | $\Theta'(0)$ | $f''(0)$ | $\Theta'(0)$ | $f''(0)$ | $\Theta'(0)$ |
| **1** | 1.41599846 | 0.71647710 | 1.41600362 | 0.71649390 | 1.41599 | 0.71845 |
| **2** | 1.44214325 | 0.88544087 | 1.44214350 | 0.88544181 | 1.44523 | 0.88453 |
| **3** | 1.4536332 | 0.96827471 | 1.45336336 | 0.96827499 | 1.45466 | 0.96825 |

## 3. Discussion

The computational study was carried out using the AB method in order to gain a physical understanding into the flow and HT features of water-based drilling NF which is composed of 3% clay and graphene NPs. The effects of physical parameters such as magnetic parameter, $M$, porosity parameter $\varepsilon_A$, the inverse Darcy parameter, $Da^{-1}$, melting heat $M_e$, the free convection parameter $\Delta_1$, and the thermal radiation parameter $Nr$ were considered. In order to obtain the desired results, the default values of these parameters were taken as follows: $M = 5$, $\varepsilon_A = 0.5 = Nr = \Delta_1$, $Da = 1 = M_e$, $\varphi = 0.03$, $\omega_1 = 0.5$, $\Theta_w = 1$, $Ec = 0.2,\ A = 0.3$. The ranges of the parameters, namely ($5 \leq M \leq 15$), ($0.5 \leq \varepsilon_A \leq 0.9$),($1 \leq Da \leq 3$), ($1 \leq M_e \leq 3$), ($0.5 \leq \Delta_1 \leq 2.5$), and ($0.5 \leq Nr \leq 2.5$), were selected as suggested in well-known studies [57–60].

In Figure 2(a),(b), the impact of the magnetic parameter ($M = 5, 10, 15$) on the velocity $f'(\eta)$ and temperature profile $\Theta(\eta)$ for both constant ($\alpha_1 = 0.0$) and variable viscosity ($\alpha_1 = 0.5$) are depicted. It is evident from Figure 2(a) that the velocity $f'(\eta)$ close to the plate decreases when the magnetic parameter increases. The decrease in $f'(\eta)$ is more dominant in the case of $\alpha_1 = 0.5$. Physically, the transverse magnetic field generates Lorentz forces, which act as a resistive force and control the fluid flow. The velocity profile is lowered as a result of the Lorentz force. The profile $\Theta(\eta)$ rises as a result of the charged fluid particles and applied magnetic field interacting (Figure 2(a)). The expectations are qualitatively supported by well-known previous results. For $\alpha_1 = 0.5$ and $\beta_1 = 0.5$, the effect of decreasing the temperature field and velocity decreases the thickness of the thermal BL and momentum when $M$ is fixed. Figure 3 (a),(b) depicts the effects of the permeability parameter $\varepsilon_A$ on the velocity and temperature profiles for both constant ($\alpha_1 = 0.0$) and variable viscosity ($\alpha_1 = 0.5$). The velocity profile increases for $\alpha_1 = 0.0$ and decreases for $\alpha_1 = 0.5$ due to the higher value of $\varepsilon_A$. The temperature characteristics show similar trends for the two distinct cases ($\alpha_1 = 0.0$ and $\alpha_1 = 0.5$). Increasing $\varepsilon_A$ results in the shrinkage of the momentum and BL thickness. Physically, the macroscopic velocity and heat transfer are primarily controlled by inertia and surface-driven dynamics rather than porous medium drag because the flow happens over a sheet with a high stretching rate. Therefore, changes in $\varepsilon_A$ only slightly change the properties of heat transmission and bulk flow. The clay NPs gain more space to accommodate the necessary postulated flow when the porosity or permeability parameters increase, which increases $f'(\eta)$. The effects of the Darcy parameter $Da$ on $f'(\eta)$ is portryed in Figure 4(a). The reduced velocity results from an increase in $Da$. Higher $Da$ results in increased permeability, which increases the fluid velocity. The velocity gradient decreases as a result of the $Da$ values. The increase in the temperature field with respect to the Darcy porosity parameter $Da$ is shown in Figure 4(b). Physically, when the Darcy $Da$ parameter increases, the porous medium's permeability increases, enabling higher fluid flow velocity and better convective heat transfer. This leads to a more effective distribution of thermal energy within the drilling NF, increasing its temperature because of decreased flow resistance and improved interaction between the NF and the porous structure. In Figure 5(a, b), the impact of the melting heat $M_e$ on $f'(\eta)$ and $\Theta(\eta)$ for a clay-based NF is explained. The melting parameter $M_e$ leads to improvements in the BL $f'(\eta)$ and the associated thickness. Physically, the phase-change procedure consumes thermal energy close to the boundary, lowering the specific fluid viscosity and improving buoyancy-driven flow while also producing a cooling effect that decreases the temperature gradient and speeds up the fluid's motion. As a result, $f'(\eta)$ increases. For removing impediments from the interior walls of the rough surfaces, like the hole bit, the melting heat is beneficial. Figure 5(b) explains how the melting factor $M_e$ affects the temperature of drilling NF. The temperature field reduces, and the thickness of the thermal BL increases as a result of increases in $M_e$. Physically, a larger melting parameter transmits heat from heated fluid to the cold wall more quickly, which leads to higher HT to the surrounding area and ultimately lowers the temperature of the NF. The influence of variable viscosity and variable thermal conductivity on $f'(\eta)$ and $\Theta(\eta)$ are dominant compared with the effects of constant parameters. Figure 6(a),(b) illustrates the influence of the free convection parameter $\Delta_1$ on $f'(\eta)$ and $\Theta(\eta)$ under both the constant and variable viscosity and variable thermal conductivity scenarios. Physically, the magnitude of $\Delta_1$ demonstrates the relative significance of free and forced convection. The augmentation of heat transfer brought on by temperature-induced density gradients in the drilling NF system is determined by the free convection parameter $\Delta_1$, which measures the relative dominance of buoyancy-driven thermal convection over inertial pulls. Figure 6(a) shows that as the buoyancy parameter $\frac{Gr}{Re^2{}_x}$ is increased, the velocity field increases and the thickness of the BL grows. Physically, $Gr > 0$ refers to assisting flow. A rise in $f'(\eta)$ is seen close to the stretching boundary and exponentially diminishes as one moves away from the BL. From a physical perspective, the free convection enables the fluid to move away from the stretching surface to the free stream. The fluid flow increases as the free stream moves upward. This reveals the velocity profile when constant thermophysical effects are considered. On the other hand, $Gr > 0$ results in a decrease in the thickness of the thermal BL, which increases the rate of HT across the surface (Figure 6(b)). The temperature profile in the case of constant thermal conductivity is lower than the variable case. The velocity and temperature profiles for various values of the radiation parameter $Nr$ are given in Figure 7(a),(b). It is clear from both figures that when $Nr$ increases, the temperature and velocity profiles inside the BL increase along with the momentum and thermal thickness. Physically, the radiation parameter has a significant impact on the temperature and velocity profiles by changing the fluid heat transfer mechanisms. As the radiation parameter rises, the thermal radiation improves the system's energy exchange, which raises the temperature profile because of more radiative heat flux. The velocity profile is impacted indirectly because the higher temperature gradients change the buoyancy forces and viscous effects, which may accelerate fluid flow in natural convection scenarios or change the properties of the BL in forced convection systems. Since the fluid temperature rises with an increase in $\beta_1$, the variance in thermal conductivity cannot be disregarded. Furthermore, the noteworthy increase in temperature indicates that the volume rate of flow at a segment perpendicular to the plate rises as $\beta_1$ grows. The vertical velocity profiles are found to decrease when the variable viscosity parameter $\alpha_1$ increases. For this reason, the thickness of the vertical velocity BL decreases as the fluid viscosity parameter $\alpha_1$ increases. This can be explained physically by the fact that a larger $\alpha_1$ indicates a greater temperature differential between the fluid's surface and the surrounding air.

The streamlines and isotherm pattern of the flow field are displayed in Figures 8(a) and 9(a) and Figures 8(b) and 9(b), respectively. The streamline patterns exhibit thicker BL and decreased flow velocity as the magnetic parameter $M$ increases. This is because the reverse Lorentz force dampens the fluid's motion. The magnetic field increases Joule heating and inhibits convective cooling, resulting in more densely packed isotherm contours close to the surface, which indicates larger temperature gradients. As a result, the thermal BL becomes hotter and loses its heat dissipation efficiency.

The comparative graphic (Figure 10) explicitly shows that the HNF (clay–graphene/water) performs better at heat transmission than the mono-NF (clay/water) by achieving a higher Nusselt number. The scattered clay and graphene NPs work in concert to boost thermal conductivity, maximize viscosity, and amplify microconvection within the boundary layer, resulting in this increase in efficiency. For drilling applications, where quick heat dissipation is essential, the HNF works better because it lowers thermal resistance and increases the energy exchange efficiency.

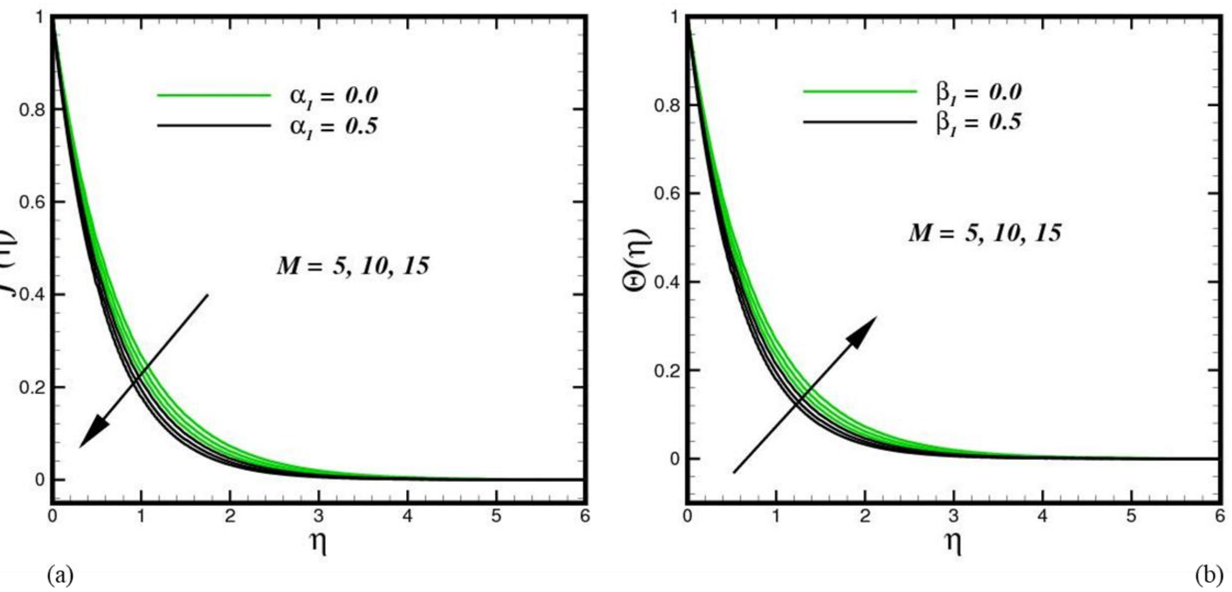


**Figure 2.** Flow and thermal field depending on $M$.

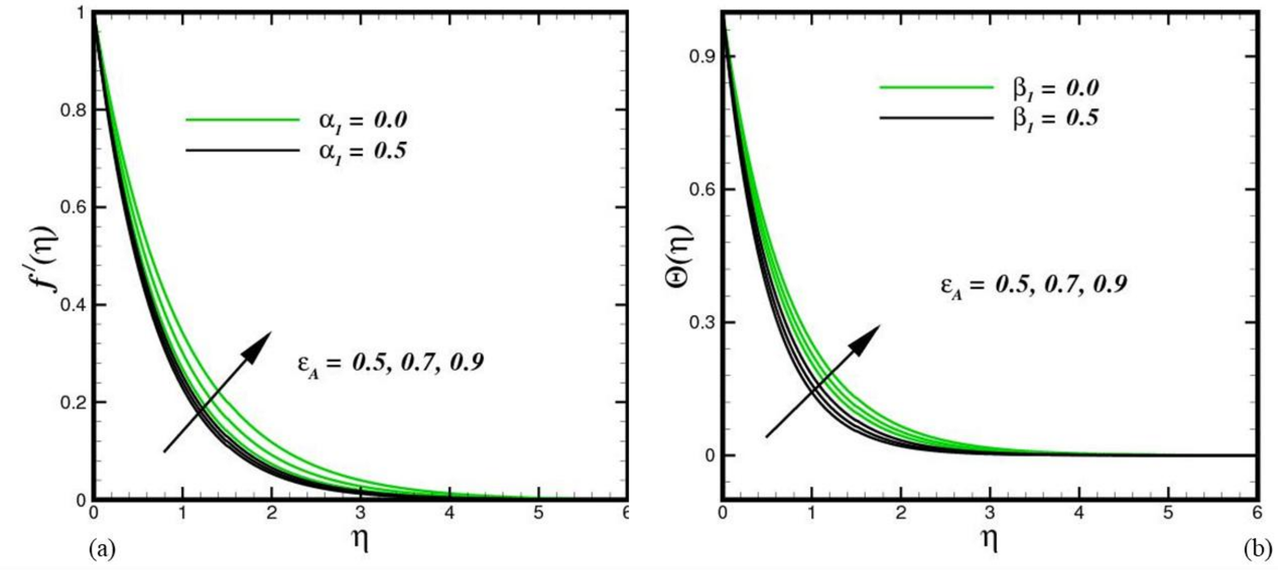


**Figure 3.** Flow and thermal field depending on $\epsilon_A$.

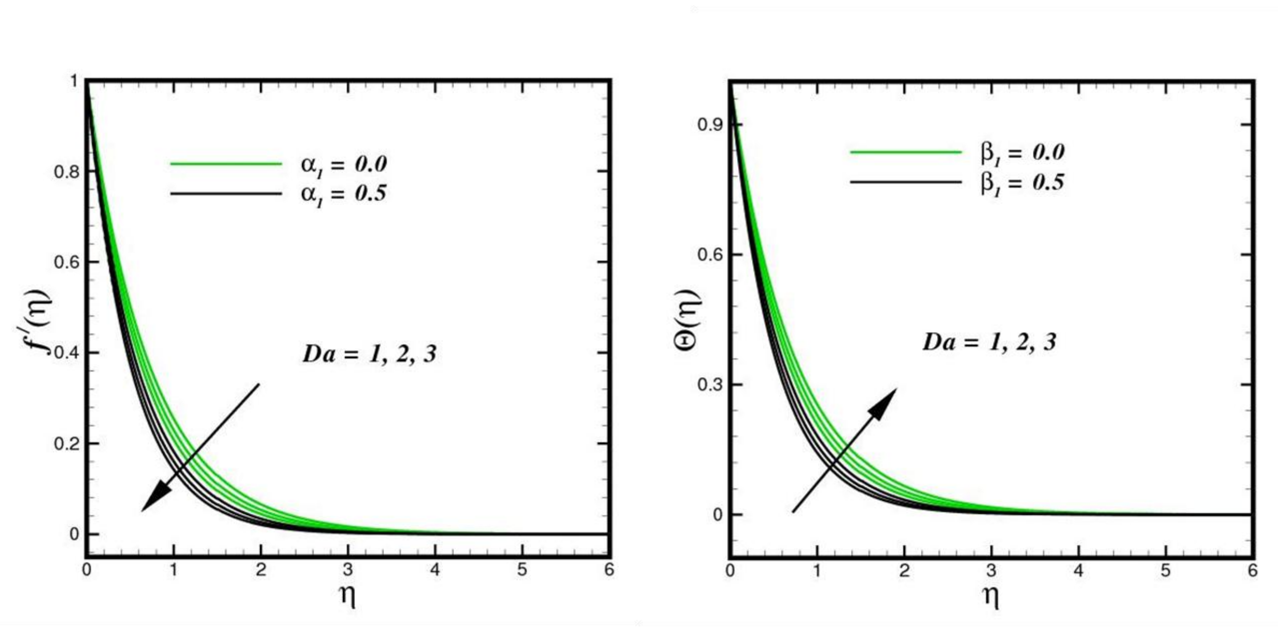


(a) (b)

**Figure 4.** Flow and thermal field depending on $Da$.

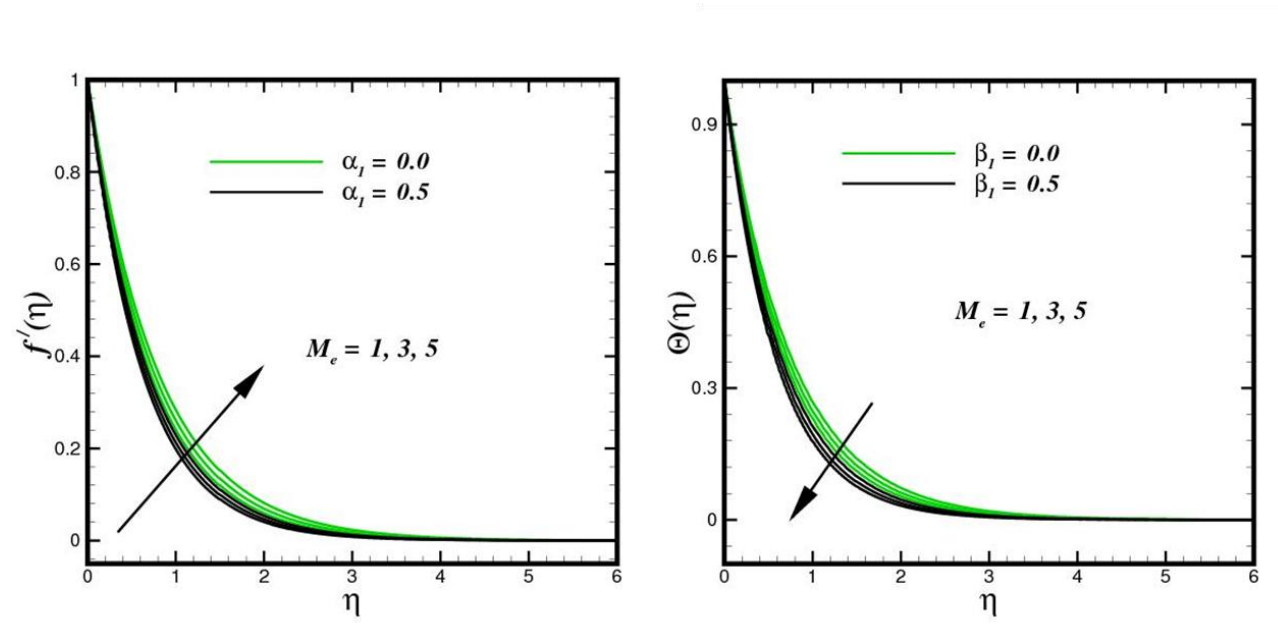


(a) (b)

**Figure 5.** Flow and thermal field depending on $M_e$.

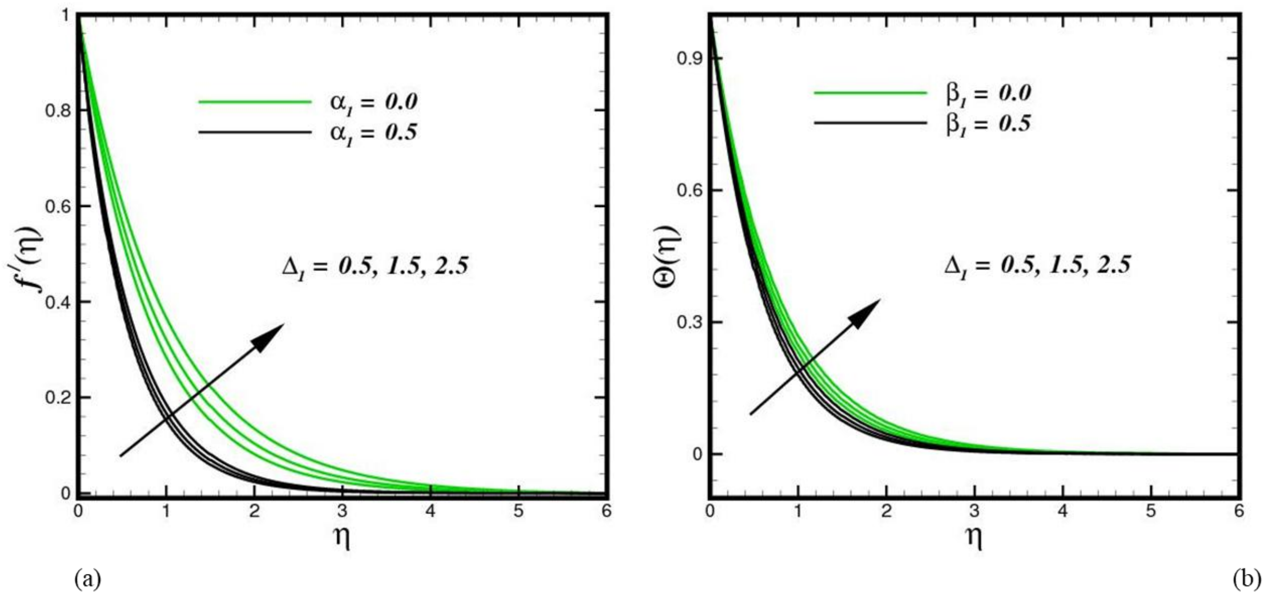


**Figure 6.** Flow and thermal field depending on $\Delta_1$.

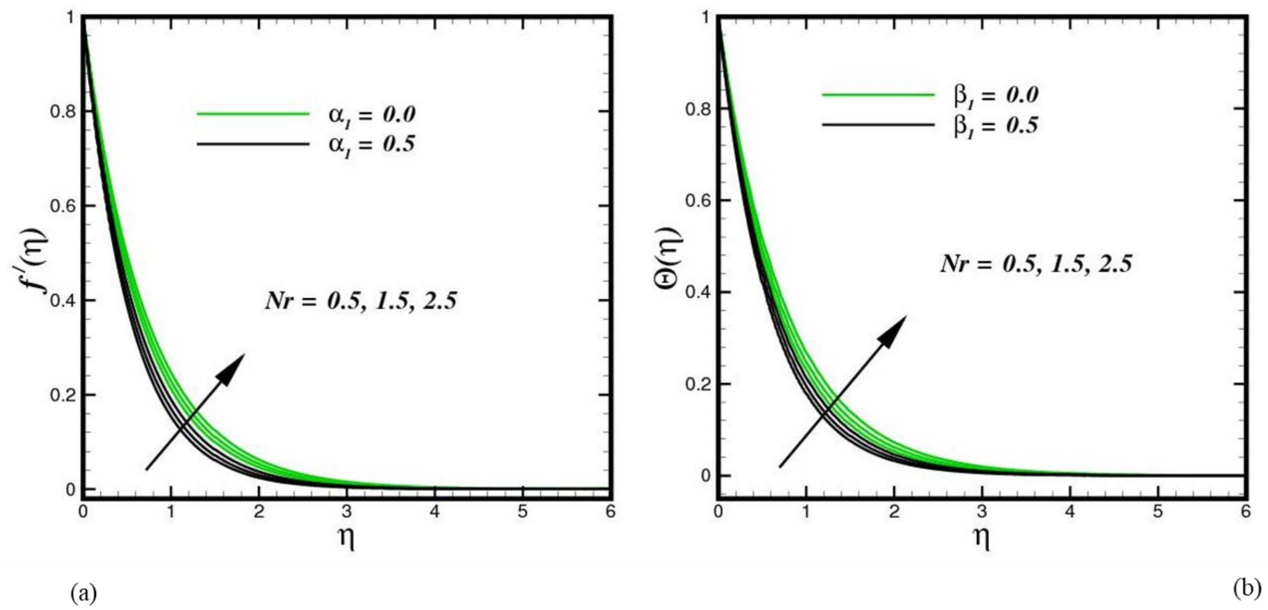


**Figure 7.** Flow and thermal field depending on $Nr$.

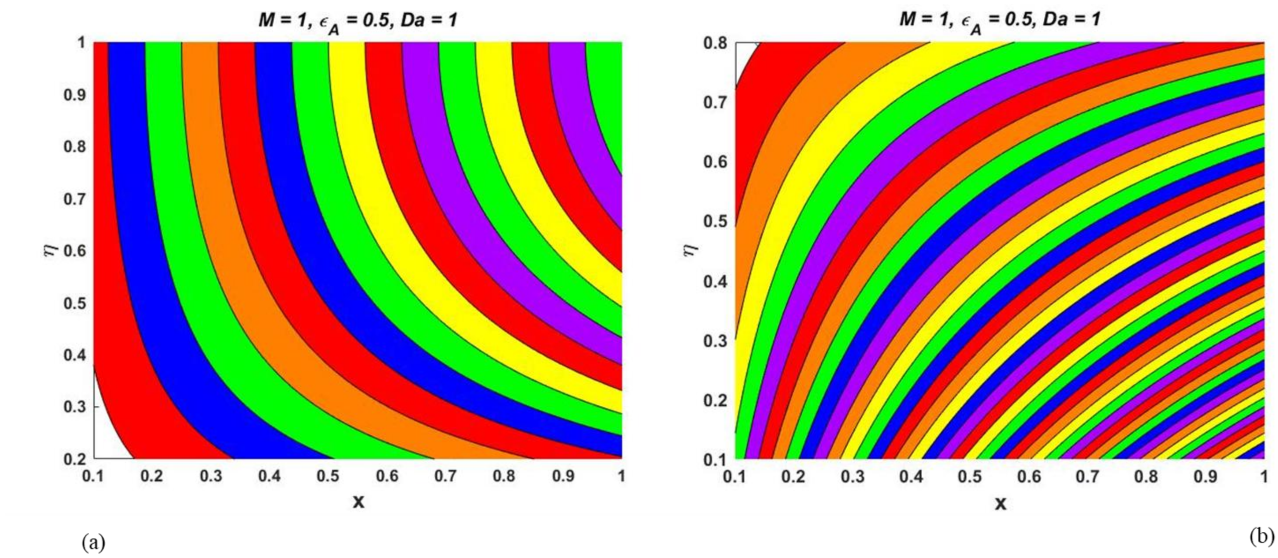


**Figure 8.** Pattern of streamlines and isotherms.

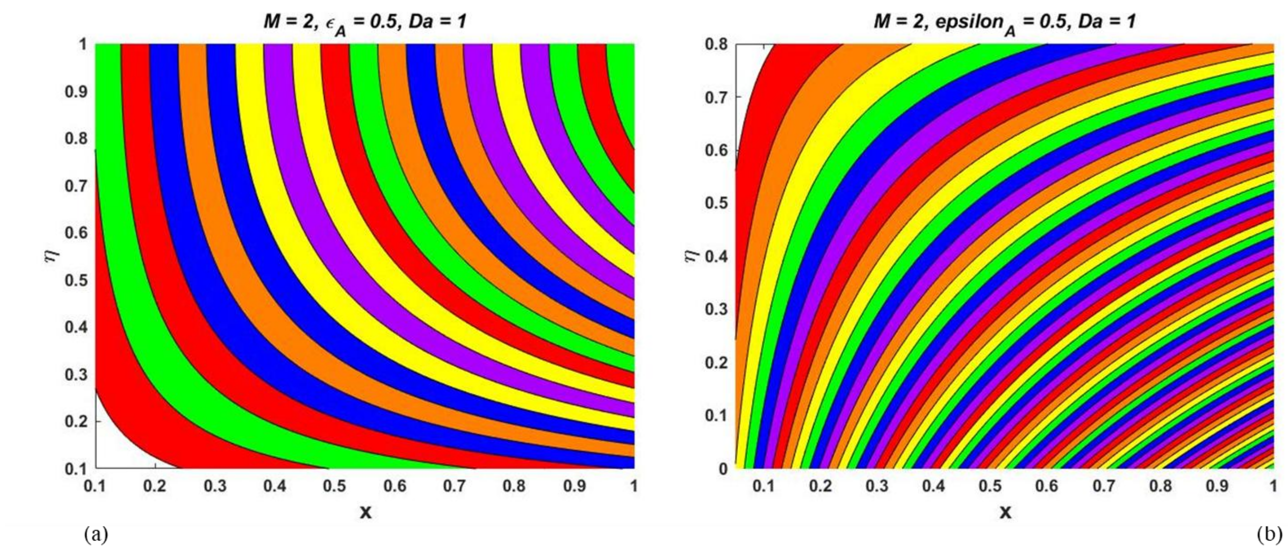


**Figure 9.** Pattern of streamlines and isotherms.

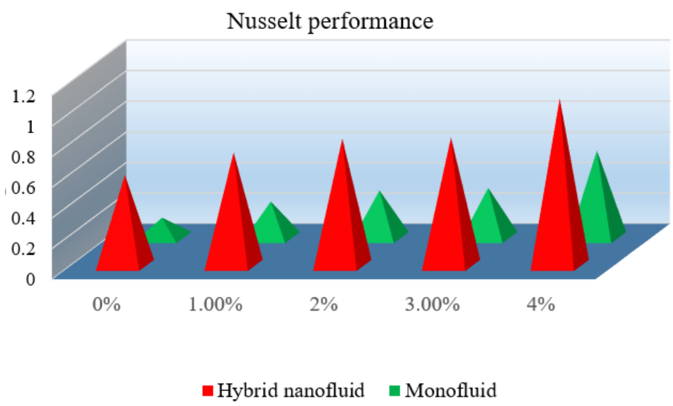


**Figure 10.** Performance of Nusselt number with mono-NF and hybrid NF, taking different loads of clay and graphene nanomaterials.

**Table 4.** Computational outcomes for $C_{fx}$ ($Go+$ clay NP-based NF) taking $\varphi=3\%$ versus selected parameters with $Pr=7.56$ and $Ec=0.5$.

| $\Delta_1$ | $\varepsilon_A$ | $Da^{-1}$ | $Nr$ | $\Theta_w$ | $A$ | $C_{fx}$ $\alpha_1=0.0$ | $C_{fx}$ $\alpha_1=0.5$ |
|---|---|---|---|---|---|---|---|
| 0.5 | 1.5 | 0.5 | 1.5 | 0.5 | 0.5 | −1.27084 | −1.01807 |
| 1 | | | | | | −1.29655 | −1.02741 |
| 1.5 | | | | | | −0.31607 | −0.29152 |
| 0.5 | 1.5 | 0.5 | 1.5 | 0.5 | 0.5 | −2.17048 | −1.10458 |
| | 0.6 | | | | | −1.19657 | −1.00168 |
| | 0.7 | | | | | −0.21709 | −1.01922 |
| 0.5 | 1.5 | 0.5 | 1.5 | 0.5 | 0.5 | −1.16788 | −1.10627 |
| | | 0.7 | | | | −1.13907 | −1.11725 |
| | | 0.9 | | | | −1.19788 | −1.12267 |
| 0.5 | 1.5 | 0.5 | 1.5 | 0.5 | 0.5 | −1.17828 | −1.19085 |
| | | | 60 | | | −1.18901 | −1.22205 |
| | | | 70 | | | −1.20919 | −1.24228 |
| 0.5 | 1.5 | 0.5 | 1.5 | 0.5 | 0.5 | −1.38272 | −1.27891 |
| | | | | 0.7 | | −1.98402 | −1.42289 |
| | | | | 0.9 | | −2.08483 | −1.80982 |
| 0.5 | 1.5 | 0.5 | 1.5 | 0.5 | 0.5 | −0.81678 | −0.48930 |
| | | | | | 0.4 | −0.76090 | −0.29801 |
| | | | | | 0.6 | −0.61087 | −0.18890 |

In this section, the numerical outcomes of the skin friction $C_{fx}$ and Nusselt coefficient $Nu_x$ for graphene + clay NP-based NF with a volume percent $\varphi=3\%$ of nanomaterials is presented in Tables 4 and 5, respectively. A comparative analysis is performed for constant and variable thermophysical features in order to check their relative performance with these parameters. The skin friction can be significantly impacted by the free convection parameter $\Delta_1$, porosity $\varepsilon_A$, inverse Darcy number $Da^{-1}$, and heat radiation $Nr$ in fluid flow conditions. In the event of variable viscosity, the fluid's permeability results in a decrease in $C_{fx}$ as the porosity and Darcy number rise, enabling smoother flow and less resistance. The thermal gradient produced by free convection and thermal radiation can nevertheless affect $C_{fx}$ with a constant viscosity, which exhibits a more uniform frictional response. Increased heat radiation has the ability to increase fluid temperatures, which could change the viscosity and, consequently, raises $C_{fx}$. The variables features considered in this problem result in intricate flow patterns that affect the functionality of systems like thermal exchangers and porous media applications in drilling operations. Thermal radiation, free convection, porosity, and the Darcy number all have a major impact on $Nu_x$, which measures convective HT in comparison with conductive HT. When viscosity varies, the Nusselt number tends to rise as temperatures rise because of the reduced viscosity, which promotes convective HT. On the other hand, when the viscosity is not constant, the Nusselt number is more stable. Large porosity promotes more fluid movement, which enhances the rate of HT. Another important factor is the Darcy number, which indicates the flow's resistance in porous media. A higher Darcy number typically improves the fluid's movement, which increases $Nu_x$. There are two different impacts of the NPs on $Nu_x$: a positive effect brought on by the NPs when variable aspects of thermal conductivity $\beta_1=0.5$ are considered and an unfavorable effect brought on by variable viscosity, when $\alpha_1 = 0.5$ is considered. At low free convection numbers, conduction HT dominates over natural convection, while convection dominates at high free convection numbers. Convection is the primary physical mechanism of HT, and the addition of NPs will make the NF more viscous, which will lessen the convection currents and, in turn, the temperature differential at the surface and $Nu_x$. Because of the variable thermal conductivity of drilling NF, this will be accompanied by a great improvement in heat transmission.

**Table 5.** Computational outcomes for $Nu_x$ ($Go$ +clay NP-based NF) taking $\varphi$ =3% versus selected parameters with $Pr = 7.56$ and $Ec = 0.5$.

| $\Delta_1$ | $\varepsilon_A$ | $Da^{-1}$ | $Nr$ | $\Theta_w$ | $Ec$ | $\omega_1$ | $A$ | $Nu_x$ $\beta_1 = 0.0$ | $Nu_x$ $\beta_1 = 0.5$ |
|---|---|---|---|---|---|---|---|---|---|
| **0.5** | 0.5 | 0.5 | 0.5 | 0.5 | 0.5 | 0.1 | 0.2 | 1.14823 | 2.05807 |
| **0.7** | | | | | | | | 1.16978 | 2.02741 |
| **0.9** | | | | | | | | 1.18923 | 2.0915 |
| **0.5** | 0.5 | 0.5 | 0.5 | 0.5 | 0.5 | 0.1 | 0.2 | 1.20179 | 1.10458 |
| | 0.6 | | | | | | | 1.22789 | 2.08168 |
| | 0.7 | | | | | | | 1.44696 | 2.01922 |
| **0.5** | 0.5 | 0.5 | 0.5 | 0.5 | 0.5 | 0.1 | 0.2 | 1.22917 | 2.10627 |
| | | 0.7 | | | | | | 1.24068 | 2.11725 |
| | | 0.9 | | | | | | 1.26875 | 2.12267 |
| **0.5** | 0.5 | 0.5 | 0.5 | 0.5 | 0.5 | 0.1 | 0.2 | 1.19988 | 2.16716 |
| | | | 0.6 | | | | | 1.18689 | 2.18816 |
| | | | 0.7 | | | | | 1.21274 | 2.19989 |
| **0.5** | 0.5 | 0.5 | 0.5 | 0.5 | 0.5 | 0.1 | 0.2 | 1.17898 | 2.19085 |
| | | | | 0.6 | | | | 1.16807 | 2.22205 |
| | | | | 0.7 | | | | 1.14046 | 2.24228 |
| **0.5** | 0.5 | 0.5 | 0.5 | 0.5 | 0.5 | 0.1 | 0.2 | 1.21078 | 2.20185 |
| | | | | | 0.5 | | | 1.9888 | 2.23446 |
| | | | | | 0.5 | | | 1.14230 | 2.29906 |
| **0.5** | 0.5 | 0.5 | 0.5 | 0.5 | 0.5 | 0.1 | 0.2 | 1.14327 | 2.67597 |
| | | | | | | 0.2 | | 1.13427 | 2.23445 |
| | | | | | | 0.3 | | 1.12008 | 2.07545 |
| **0.5** | 0.5 | 0.5 | 0.5 | 0.5 | 0.5 | 0.1 | 0.2 | 1.43562 | 1.78904 |
| | | | | | | | 0.8 | 1.32745 | 1.43325 |
| | | | | | | | `1.6 | 1.03359 | 1.68767 |

## 4. Conclusions

This study examined the anomalous heat transfer in a mixed convection flow of water-based drilling NF containing clay and graphene over a vertically extended plate in a Darcy–Brinkman permeable medium. The effects of free convection, Darcy number, porosity, magnetic effects temperature-dependent viscosity, thermal conductivity, melting heat, nonlinear radiation, and frictional heating were included in this study. Using a multi-step computational Adams–Bashforth-based predictor–corrector technique, governing equations are solved. The study analyzes the Nusselt numbers and frictional drag coefficients, taking constant versus variable viscosity and thermal conductivity into account. This discussion shows that the results can be used practically to improve drilling fluid's performance and deepen the comprehension of heat transfer in intricate fluid systems. The following inferences can be made from the current study.

- The BLF is regulated by increasing the magnetic parameter, while anomalous rises in temperature against the magnetic parameter are seen.
- The velocity and temperature of the NF show similar behavior with modified porosity parameters. A nearly similar trend was seen for radiative and free convection and the Darcy number.
- The local skin–friction coefficient rises with the free convection parameter, while the opposite trend emerges for magnetic and porosity parameters.
- The action of the Darcy number on velocity is discouraging, while opposite behavior was seen for melting heat. A conflicting effect was observed for temperature.
- The Nusselt number declines with an increase in the magnetic, Darcy, porosity, and melting parameters.
- Variable thermophysical features have a greater tendency to regulate fluid velocity as compared with constant features.
- The variable properties can improve the general effectiveness of fluid systems, particularly in applications involving complex fluid behavior, such as thermal management in engineering systems.
- Variable viscosity has a significant impact on skin friction and the heat transfer rate because they can change the flow characteristics and the BL's behavior, resulting in lower skin friction coefficients, while variable thermal conductivity affects the temperature gradient at the surface, allowing high heat transfer rates.

**Study limitations:** The Brinkman–Maxwell–Garnett model, which may not adequately represent the intricate interface's interplay and the aggregation effects of NPs in drilling NF, is one of the study's limitations. Furthermore, because the AB approach is explicit, it could introduce stability limitations and necessitate fine grid resolutions for convergence, which would increase the computing cost. The study is limited in its applicability to forced convection or mixed convection scenarios because it focuses primarily on free convection. Furthermore, the impact of surface changes, clustering, and NP shape on heat transfer characteristics is not specifically taken into account, which may affect how accurately estimations of thermophysical properties are made.

**Future recommendations:** Future research will enhance this study by including sophisticated NF models that take interfacial effects and NP aggregation into consideration. This would increase the precision of thermophysical property estimations. The computational method could be combined with machine learning techniques or expanded to implicit methods to improve grid reliance and stability. The practical usefulness of the results would be strengthened by experimental validation under practical drilling settings. Further research on the effects of hybrid convection scenarios (mixed/forced) and NP morphologies (such as rods and platelets) may further shed light on how to best optimize drilling fluid's performance. Investigating turbulent regimes and temporal flow dynamics would increase the study's applicability to industry.

## Use of Generative AI tools declaration

The author declares they have not used artificial intelligence (AI) tools in the creation of this article.

## Conflict of interest

The authors of this manuscript have no conflict of interest

## References


1. K. Hiemenz, Die Grenzschicht an einem in den gleichformigen Flussigkeitsstrom eingetauchten geraden Kreiszylinder, *Dinglers Polytech. J.*, **326** (1911), 311. Available from: https://cir.nii.ac.jp/crid/1573668924607721856.
2. F. Homann, Der Einfluß großer Zähigkeit bei der Strömung um den Zylinder und um die Kugel, *ZAMM*, **16** (1936), 153–164. https://doi.org/10.1002/zamm.19360160304
3. L. Howarth F. R. S., CXLIV. The boundary layer in three dimensional flow.—Part II. The flow near a stagnation point, *London, Edinburgh Dublin Philos. Mag. J. Sci.*, **42** (2009), 1433–1440. https://doi.org/10.1080/14786445108560962
4. A. Davey, D. Schofield, Three-dimensional flow near a two-dimensional stagnation point, *J. Fluid Mech.*, **28** (1967), 149–151. https://doi.org/10.1017/S0022112067001958
5. N. Bachok, A. Ishak, I. Pop, Boundary layer stagnation-point flow and heat transfer over an exponentially stretching/shrinking sheet in a nanofluid, *Int. J. Heat Mass Transfer*, **55** (2012), 8122–8128. https://doi.org/10.1016/j.ijheatmasstransfer.2012.08.051
6. G. C. Dash, R. S. Tripathy, M. M. Rashidi, S. R. Mishra, Numerical approach to boundary layer stagnation-point flow past a stretching/shrinking sheet, *J. Mol. Liq.*, **221** (2016), 860–866. https://doi.org/10.1016/j.molliq.2016.06.072
7. L. Ali, R. Apsari, A. Abbas, P. Tak, Entropy generation on the dynamics of volume fraction of nano-particles and coriolis force impacts on mixed convective nanofluid flow with significant magnetic effect, *Numer. Heat Transfer, Part A: Appl.*, 2024, 1–16, https://doi.org/10.1080/10407782.2024.2360652
8. S. U. S. Choi, J. A. Eastman, Enhancing thermal conductivity of fluids with nanoparticles, 1995. Available from: https://ecotert.com/pdf/196525_From_unt-edu.pdf.
9. C. Liu, M. Khan, M. Ramzan, Y. Chu, S. Kadry, M. Y. Malik, et al., Nonlinear radiative Maxwell nanofluid flow in a Darcy–Forchheimer permeable media over a stretching cylinder with chemical reaction and bioconvection, *Sci. Rep.*, **11** (2021), 9391. https://doi.org/10.1038/s41598-021-88947-5
10. P. K. Pattnaik, S. R. Mishra, O. Anwar Bég, U. F. Khan, J. C. Umavathi, Axisymmetric radiative titanium dioxide magnetic nanofluid flow on a stretching cylinder with homogeneous/heterogeneous reactions in Darcy-Forchheimer porous media: Intelligent nanocoating simulation, *Mater. Sci. Eng.: B*, **277** (2022), 115589. https://doi.org/10.1016/j.mseb.2021.115589
11. A. M. Sedki, Effect of thermal radiation and chemical reaction on MHD mixed convective heat and mass transfer in nanofluid flow due to nonlinear stretching surface through porous medium, *Results Mater.*, **16** (2022), 100334. https://doi.org/10.1016/j.rinma.2022.100334
12. N. Anjum, W. A. Khan, A. Hobiny, M. Azam, M. Waqas, M. Irfan, Numerical analysis for thermal performance of modified Eyring Powell nanofluid flow subject to activation energy and bioconvection dynamic, *Case Stud. Therm. Eng.*, **39** (2022), 102427. https://doi.org/10.1016/j.csite.2022.102427

13. Y. Bai, Q. Tang, Y. Zhang, Unsteady MHD oblique stagnation slip flow of Oldroyd-B nanofluids by coupling Cattaneo-Christov double diffusion and Buongiorno model, *Chinese J. Phys.*, **79** (2022), 451–470. https://doi.org/10.1016/j.cjph.2022.09.013
14. M. I. Asjad, M. Zahid, M. Inc, D. Baleanu, B. Almohsen, Impact of activation energy and MHD on Williamson fluid flow in the presence of bioconvection, *Alex. Eng. J.*, **61** (2022), 8715–8727. https://doi.org/10.1016/j.aej.2022.02.013
15. F. Mabood, M. D. Shamshuddin, S. R. Mishra, Characteristics of thermophoresis and Brownian motion on radiative reactive micropolar fluid flow towards continuously moving flat plate: HAM solution, *Math. Comput. Simul.*, **191** (2022), 187–202. https://doi.org/10.1016/j.matcom.2021.08.004
16. S. A. Khan, T. Hayat, A. Alsaedi, B. Ahmad, Heat and mass transfer enhancement in nonlinear mixed convective flow: Buongiorno model and melting heat phenomenon, *Int. Commun. Heat Mass Transfer*, **153** (2024), 107330. https://doi.org/10.1016/j.icheatmasstransfer.2024.107330
17. S. Rehman, M. Boujelbene, M. Waqas, On the augmentation of heat transfer with hybrid nanofluid containing microorganisms on flat plate under thermal radiation, using mixtures models, *Energy Environ.*, 2024. https://doi.org/10.1177/0958305X241244487
18. J. Tian, S. Rehman, M. Saqib, A. G. Shah, T. H. AlAbdulaal, Entropy generation and heat transport performance of a partially ionized viscoelastic tri-hybrid nanofluid flow over a convectively heated cylinder, *Case Stud. Therm. Eng.*, **60** (2024), 104623. https://doi.org/10.1016/j.csite.2024.104623
19. S. Shen, S. Rehman, S. O. Shah, F. Albouchi, S. Rauf, Entropy optimization and heat transfer in thin film flow of electromagnetic micropolar nanofluid using Maxwell–Bruggeman and Krieger–Dougherty models, *Alex. Eng. J.*, **106** (2024), 71–86. https://doi.org/10.1016/j.aej.2024.06.075
20. J. Abdo, M. D. Haneef, Clay nanoparticles modified drilling fluids for drilling of deep hydrocarbon wells, *Appl. Clay Sci.*, **86** (2013), 76–82. https://doi.org/10.1016/j.clay.2013.10.017
21. I. Khan, A. Hussanan, M. Saqib, S. Shafie, Convective Heat Transfer in Drilling Nanofluid with Clay Nanoparticles: Applications in Water Cleaning Process, *BioNanoSci.*, **9** (2019), 453–460. https://doi.org/10.1007/s12668-019-00623-1
22. G. Cheraghian, Application of Nano-Particles of Clay to Improve Drilling Fluid, *Int. J. Nanosci. Nanotechnol.*, **13** (2017), 177–186.
23. K. S. Nisar, D. Khan, A. Khan, W. A. Khan, I. Khan, A. M. Aldawsari, Entropy Generation and Heat Transfer in Drilling Nanoliquids with Clay Nanoparticles, *Entropy*, **21** (2019), 1226. https://doi.org/10.3390/e21121226
24. S. Elattar, U. Khan, A. Zaib, A. Ishak, N. Alwadai, H. Albalawi, Radiative flow of clay nanoparticles on the lubricity of Williamson drilling fluids across a vertical surface in a Darcy-Brinkman porous medium, *Chinese J. Phys.*, **92** (2024), 701–720. https://doi.org/10.1016/j.cjph.2024.08.031
25. H. A. Isede, A. Adeniyan, Mixed convection flow and heat transfer of chemically reactive drilling liquids with clay nanoparticles subject to radiation absorption, *Ain Shams Eng. J.*, **12** (2021), 4167–4180. https://doi.org/10.1016/j.asej.2021.04.030
26. A. Ali, M. I. Asjad, M. Usman, M. Inc, Numerical Solutions of a Heat Transfer for Fractional Maxwell Fluid Flow with Water Based Clay Nanoparticles; A Finite Difference Approach, *Fractal Fract.*, **5** (2021), 242. https://doi.org/10.3390/fractalfract5040242

27. J. Kayalvizhi, A. G. V. Kumar, H. F. Öztop, N. Sene, N. H. Abu-Hamdeh, Heat Transfer Enhancement through Thermodynamical Activity of H2O/Clay Nanofluid Flow over an Infinite Upright Plate with Caputo Fractional-Order Derivative, *Energies*, **15** (2022), 6082. https://doi.org/10.3390/en15166082
28. L. Ali, P. Kumar, H. Poonia, S. Areekara, R. Apsari, The significant role of Darcy–Forchheimer and thermal radiation on Casson fluid flow subject to stretching surface: A case study of dusty fluid, *Mod. Phys. Lett. B*, **38** (2024), 2350215. https://doi.org/10.1142/S0217984923502159
29. S. Mukhopadhyay, Natural convection flow on a sphere through porous medium in presence of heat source/sink near a stagnation point, *Math. Modell. Anal.*, **13** (2008), 513–520. https://doi.org/10.3846/1392-6292.2008.13.513-520
30. H. Rosali, A. Ishak, I. Pop, Mixed Convection Stagnation-Point Flow Over a Vertical Plate with Prescribed Heat Flux Embedded in a Porous Medium: Brinkman-Extended Darcy Formulation, *Transp. Porous. Med.*, **90** (2011), 709–719. https://doi.org/10.1007/s11242-011-9809-7
31. S. Mukhopadhyay, Upper-Convected Maxwell Fluid Flow over an Unsteady Stretching Surface Embedded in Porous Medium Subjected to Suction/Blowing, *Zeitschrift für Naturforschung A*, **67** (2012), 641–646. https://doi.org/10.5560/zna.2012-0075
32. Q. Wang, K. Wang, P. Li, Forced convective heat and mass transfer in a bidisperse porous parallel-plate channel with a first order reaction on the wall, *Therm. Sci. Eng. Prog.*, **13** (2019), 100369. https://doi.org/10.1016/j.tsep.2019.100369
33. A. Zaib, R. U. Haq, A. J. Chamkha, Mixed convective flow of a Casson fluid over a vertical plate in Darcy-Brinkman porous medium with slips, *JPM*, **24** (2021), 1–11. https://doi.org/10.1615/JPorMedia.2020025172
34. C. Y. Wang, Darcy-Brinkman flow in a rotating channel filled with an anisotropic porous medium, *JPM*, **25** (2022), 31–40. https://doi.org/10.1615/JPorMedia.2021038567
35. A. Adil, T. Baig, F. Jamil, M. Farhan, M. Shehryar, H. M. Ali, et al., Nanoparticle-based cutting fluids in drilling: A recent review, *Int. J. Adv. Manuf. Technol.*, **131** (2024), 2247–2264. https://doi.org/10.1007/s00170-023-11048-2
36. M. Al-Shargabi, S. Davoodi, D. A. Wood, A. Al-Musai, V. S. Rukavishnikov, K. M. Minaev, Nanoparticle applications as beneficial oil and gas drilling fluid additives: A review, *J. Mol. Liq.*, **352** (2022), 118725. https://doi.org/10.1016/j.molliq.2022.118725
37. A. Razaq, T. Hayat, S. A. Khan, Entropy generated nonlinear mixed convective beyond constant characteristics nanomaterial wedge flow, *Int. Commun. Heat Mass Transfer*, **159** (2024), 108000. https://doi.org/10.1016/j.icheatmasstransfer.2024.108000
38. T. Gupta, A. K. Pandey, M. Kumar, Numerical study for temperature-dependent viscosity based unsteady flow of GP-$MoS_2$/$C2H_6O_2$-$H_2O$ over a porous stretching sheet, *Numer. Heat Transfer, Part A: Appl.*, **85** (2024), 1063–1084. https://doi.org/10.1080/10407782.2023.2195689
39. M. Farooq, A. Anjum, S. Rehman, M. Y. Malik, Entropy analysis in thermally stratified Powell-Eyring magnesium-blood nanofluid convection past a stretching surface, *Int. Commun. Heat Mass Transfer*, **138** (2022), 106375. https://doi.org/10.1016/j.icheatmasstransfer.2022.106375
40. S. Rehman, Z. khan, H. Ali, U. Riaz, F. Albouchi, Role of nanomaterial on irreversibility and heat transport due to stretching surface driven blood flow in the view of Buongiorno and Tiwari-Das models, *Ain Shams Eng. J.*, **15** (2024), 102747. https://doi.org/10.1016/j.asej.2024.102747

41. S. Rehman, M. Shamshad, S. Nasr, S. Abdullaev, Thermal characteristics of MHD $CoFe_2O_4$/ water nanofluids flow past a stretching/shrinking wedge in the view of Cattaneo-Christov heat flux, *Case Stud. Therm. Eng.*, **56** (2024), 104225. https://doi.org/10.1016/j.csite.2024.104225
42. N. Khemiri, S. Rehman, T. Saidani, V. Tirth, Heat transfer analysis of radiated thin-film flow of couple-stress nanofluid embedded in a Darcy-Forchheimer medium with Newtonian heating effects, *Nucl. Eng. Technol.*, **57** (2025), 103510. https://doi.org/10.1016/j.net.2025.103510
43. A. Mishra, Analysis of radiative Ellis hybrid nanofluid flow over a stretching/shrinking cylinder embedded in a porous medium with slip condition, *Multiscale Multidiscip.*, *Model. Exp. Des.*, **8** (2025), 282. https://doi.org/10.1007/s41939-025-00871-7
44. A. Mishra, Analysis of waste discharge concentration in radiative hybrid nanofluid flow over a stretching/shrinking sheet with chemical reaction, *Mech. Time-Depend. Mater.*, **29** (2024), 7. https://doi.org/10.1007/s11043-024-09752-x
45. A. Alsaedi, S. A. Khan, T. Hayat, Cattaneo-Christov double diffusive and model development for entropy optimized flow of Reiner-Rivlin material in thermal system and environmental effect, *Alex. Eng. J.*, **72** (2023), 67–82. https://doi.org/10.1016/j.aej.2023.03.079
46. C. M. Mohana, B. R. Kumar, Shape effects of Darcy–Forchheimer unsteady three-dimensional CdTe-C/$H_2O$ hybrid nanofluid flow over a stretching sheet with convective heat transfer, *Phys. Fluids*, **35** (2023), 092002. https://doi.org/10.1063/5.0168503
47. N. M. Hafez, E. N. Thabet, Z. Khan, A. M. Abd-Alla, S. H. Elhag, Electroosmosis-modulated Darcy–Forchheimer flow of Casson nanofluid over stretching sheets in the presence of Newtonian heating, *Case Stud. Therm. Eng.*, **53** (2024), 103806. https://doi.org/10.1016/j.csite.2023.103806
48. A. Rehman, D. Khan, I. Mahariq, M. Abdelghany Elkotb, T. Elnaqeeb, Viscous dissipation effects on time-dependent MHD Casson nanofluid over stretching surface: A hybrid nanofluid study, *J. Mol. Liq.*, **408** (2024), 125370. https://doi.org/10.1016/j.molliq.2024.125370
49. M. J. Babu, N. Sandeep, 3D MHD slip flow of a nanofluid over a slendering stretching sheet with thermophoresis and Brownian motion effects, *J. Mol. Liq.*, **222** (2016), 1003–1009. https://doi.org/10.1016/j.molliq.2016.08.005
50. S. E. Awan, M. Awais, M. Asif, Z. Raja, N. Parveen, H. M. Ali, et al., Numerical Treatment for Dynamics of Second Law Analysis and Magnetic Induction Effects on Ciliary Induced Peristaltic Transport of Hybrid Nanomaterial, *Front. Phys.*, **9** (2021), 631903. https://doi.org/10.3389/fphy.2021.631903
51. S. E. Awan, M. A. Z. Raja, F. Gul, Z. A. Khan, A. Mehmood, M. Shoaib, Numerical Computing Paradigm for Investigation of Micropolar Nanofluid Flow Between Parallel Plates System with Impact of Electrical MHD and Hall Current, *Arab. J. Sci. Eng.*, **46** (2021), 645–662. https://doi.org/10.1007/s13369-020-04736-8
52. S. Nadeem, S. Ashiq, M. Ali, Williamson Fluid Model for the Peristaltic Flow of Chyme in Small Intestine, *Math. Probl. Eng.*, **2012** (2012), 479087. https://doi.org/10.1155/2012/479087
53. K. A. Khan, M. Vivas-Cortez, K. Ishfaq, M. F. Javed, N. Raza, K. S. Nisar, et al., Exploring the numerical simulation of Maxwell nanofluid flow over a stretching sheet with the influence of chemical reactions and thermal radiation, *Results Phys.*, **60** (2024), 107635. https://doi.org/10.1016/j.rinp.2024.107635
54. T. Hayat, M. Farooq, A. Alsaedi, Z. Iqbal, Melting Heat Transfer in the Stagnation Point Flow of Powell–Eyring Fluid, *J. Thermophys. Heat Transfer*, **27** (2013), 761–766. https://doi.org/10.2514/1.T4059

55. A. S. Dogonchi, D. D. Ganji, Effect of Cattaneo–Christov heat flux on buoyancy MHD nanofluid flow and heat transfer over a stretching sheet in the presence of Joule heating and thermal radiation impacts, *Indian J. Phys.*, **92** (2018), 757–766. https://doi.org/10.1007/s12648-017-1156-2
56. M. M. Rashidi, M. Ali, N. Freidoonimehr, B. Rostami, M. A. Hossain, Mixed convective heat transfer for MHD viscoelastic fluid flow over a porous wedge with thermal radiation. *Adv. Mech. Eng.*, **6** (2014), 735939. https://doi.org/10.1155/2014/735939
57. R. J. P. Gowda, R. N. Kumar, B. C. Prasannakumara, B. Nagaraja, B. J. Gireesha, Exploring magnetic dipole contribution on ferromagnetic nanofluid flow over a stretching sheet: An application of Stefan blowing, *J. Mol. Liq.* **335** (2021), 116215. https://doi.org/10.1016/j.molliq.2021.116215
58. M. Waqas, S. Jabeen, T. Hayat, M. I. Khan, A. Alsaedi, Modeling and analysis for magnetic dipole impact in nonlinear thermally radiating Carreau nanofluid flow subject to heat generation, *J. Magn. Magn. Mater.*, **485** (2019), 197–204. https://doi.org/10.1016/j.jmmm.2019.03.040
59. N. Khemiri, S. Rehman, T. Saidani, V. Tirth, Heat transfer analysis of radiated thin-film flow of couple-stress nanofluid embedded in a Darcy-Forchheimer medium with Newtonian heating effects, *Nucl. Eng. Technol.*, **57** (2025), 103510. https://doi.org/10.1016/j.net.2025.103510
60. S. Rehman, Boundary layer slip flow and heat-mass transfer of radiated water based nanofluid over a permeable disk: Darcy-Forchheimer model and activation energy, *Chaos, Solitons Fractals*, **192** (2025), 116097. https://doi.org/10.1016/j.chaos.2025.116097